

Energy Evolution Mechanism of Air Shock Wave Propagation and Attenuation Based on VMD–HT Energy Spectrum

W. Shang[†], Z. Huang, X. Zu, Q. Xiao and X. Jia

Nanjing University of Science and Technology, Nanjing, Jiangsu, 210094, China

[†]Corresponding Author Email: ammosw0257@njust.edu.cn

(Received September 18, 2021; accepted February 25, 2022)

ABSTRACT

Energy spectrum is an important tool for reflecting time–frequency characteristics of signals. The energy spectra of air shock wave at different explosion distances were analyzed to investigate the energy evolution mechanism in the propagation and attenuation process. Waveforms of air shock wave were obtained from explosion tests and numerical simulations. Energy propagation and attenuation mechanisms of air shock wave were discussed on the basis of the wave theory of fluid. Instantaneous and marginal energy spectra of air shock wave were calculated using variational modal decomposition (VMD) and Hilbert transform (HT). Energy evolution laws of air shock wave with time, frequency, and explosion distance were analyzed according to the statistical results of the energy spectra. Results showed that the instantaneous energy peak of air shock wave is directly proportional to the square of its pressure peak while inversely proportional to the third power of propagation distance. Nonlinear attenuation of air shock wave will cause frequency dispersion and decelerate the attenuation rate of the total energy of air shock wave. The energy evolution laws of air shock wave with time and frequency reflected by instantaneous and marginal energy spectra were consistent with the theoretical analysis results.

Keywords: Air shock wave; Energy evolution; Wave propagation and attenuation; Variational modal decomposition (VMD); Hilbert transform (HT); Energy spectrum.

NOMENCLATURE

c	wave velocity	p	pressure
c_p	constant-pressure specific heat	P_{CJ}	C-J pressure of explosive
c_v	constant-volume specific heat	p_{top}	pressure peak
D	detonation velocity	R	explosion distance
E	total energy density	s	entropy
E_k	kinetic energy	t	time
E_p	potential energy	t_{pos+}	positive duration
ES	marginal energy spectrum	u	sub-signals
e	specific energy	v	particle velocity
e_0	initial specific internal energy	β	absorption attenuation coefficient
I	average energy flow density	ε_{ef}	equivalent displacement
IE	instantaneous energy spectrum	ϕ	phase
IE_{top}	instantaneous energy peak	φ	frequency
i	the sign of sub-signals	ρ	density
j	imaginary unit	χ	heat conduction absorption coefficient
k	adiabatic exponent	ω	energy flow density

1. INTRODUCTION

Frequent accidental explosions in recent years have caused serious damage to buildings and threatened the safety of people's lives. Air shock wave is a form of explosion damage effect. Propagation and attenuation mechanisms of air shock wave have attracted considerable research attention. Time-domain characteristics of air shock wave have been extensively investigated. [Friedlander \(1946\)](#) proposed a two-parameter ideal pressure–time history function of shock wave to describe characteristics of shock wave with pressure and positive phase duration. [Thornhill \(1959\)](#) modified Friedlander's formula by introducing an attenuation factor to improve the description of overpressure–time histories for solid explosives. In engineering applications, the air shock wave is often simplified as an approximate triangular pulse ([UFC-3-340-02, 2008](#)). In the calculation of the air shock wave parameters, [Brode \(1955\)](#), [Henrych \(1979\)](#), [Held \(1983a\)](#), and [Kinney and Graham \(1985\)](#) fitted the relationship among peak overpressure, positive duration, positive phase impulse, and scaled distance using a large number of explosion tests and numerical simulations. [Hopkinson and Cranz](#) investigated the geometric similarity phenomenon in the propagation of air shock wave ([Goel 2015](#)). [Anderson *et al.* \(2000\)](#), [Maiz *et al.* \(2016\)](#), and [Li *et al.* \(2018\)](#) reported the effect of composite and double-layer charges on propagation characteristics of air shock wave. [Fouchier *et al.* \(2017\)](#), [Bowles *et al.* \(2012\)](#), [Izadifard *et al.* \(2010\)](#), and [Silnikov *et al.* \(2015\)](#) analyzed propagation laws of air shock wave in complex environments, such as city streets and high altitude. [Artero-Guerrero *et al.* \(2017\)](#) and [Simoens and Lefebvre \(2015\)](#) carried out experiments and simulations to explore the influence of charge shape on air shock wave. These studies are based on time-domain characteristic parameters of air shock wave. However, time domain analysis fails to provide frequency domain information, such as frequency component, frequency distribution range, energy distribution of each component, and frequency value of main amplitude and energy distribution.

[Held \(1983b\)](#) analyzed the damage experiments of different targets under blast load and confirmed that the damage effect of shock wave on targets is related to the closeness of their frequencies. [Coopper \(1989\)](#) investigated blast injuries and revealed that waves with different frequencies present varying injury mechanisms to the human body. High-frequency waves may result in the local rupture of organs and cause serious damage to air-containing organs, such as lungs and bowels, whereas low-frequency waves deform the organs as a whole and cause more serious damage to the trunk. [Wang *et al.* \(2017\)](#) and [Zhang *et al.* \(2020\)](#) introduced locally resonant particles to the matrix materials and attenuated the high-frequency shock wave through the scattering of particles to the shock wave and resonance between them. These studies should be based on the known frequency domain information of air shock wave. Existing studies on the frequency domain characteristics of air shock wave have presented

preliminary progress. [Li *et al.* \(2019\)](#) examined time–frequency distribution laws of air shock wave energy using wavelet analysis. [Kong *et al.* \(2010\)](#) reported the energy spectrum of air shock wave under different charges and explosion distances on the basis of wavelet packet decomposition. [Li *et al.* \(2017\)](#) improved the Hilbert energy spectrum extraction method via wavelet packet decomposition and determined the distribution of shock wave energy in time and frequency. [Hong *et al.* \(2020\)](#) analyzed the evolution of energy spectrum of composite charges with different length–diameter ratios. However, practical application of these studies has been limited because these processing methods of air shock wave signal lack correspondence with air shock wave propagation theory.

In this study, the energy spectra of air shock wave at different explosion distances were analyzed to investigate the energy distribution laws in propagation process. Waveforms of air shock wave at different explosion distances were obtained using explosion tests and numerical simulations. The energy evolution mechanism of air shock wave propagation and attenuation were discussed on the basis of the wave theory of fluid. Furthermore, the instantaneous and marginal energy spectra of air shock wave under different explosion distances were calculated using variational modal decomposition (VMD) algorithm and Hilbert transform. Finally, evolution laws of air shock wave energy with time, frequency, and explosion distance were analyzed according to the statistical results of the energy spectra.

2. PRINCIPLE OF ENERGY SPECTRUM CALCULATION

The air shock wave fails to meet applicable conditions of Hilbert transform due to its typical non-stationary random signal characterized of a wide frequency band and easy mutation ([Huang and Wu 2008](#)). According to the principle of harmonic analysis, any wave can be regarded as the superposition of several linear harmonic signals. Hence, the applicability of Hilbert transform can be solved using signal decomposition, and the energy spectrum of air shock wave can be calculated via Hilbert transform.

2.1 Signal Decomposition

The VMD algorithm aims to decompose a real-value input signal into a discrete number of sub-signals (modes). The sub-signals are often called intrinsic mode functions (IMFs). The input signal is decomposed into a set of amplitude-modulated–frequency-modulated (AM–FM) signals by screening the frequency dominant signal. The sum of the estimated bandwidth of IMF signals must be minimized to realize the adaptive decomposition of the input signal ([Dragomiretskiy and Zosso 2014](#)). Discrete process of waveforms will inevitably cause Gibbs effect, and energy leakage and modal overlap will occur in the local signal. However, the VMD algorithm effectively reduces the Gibbs effect by

centralizing the frequency of the component signal. Thus, the accuracy of the signal processing result is enhanced. According to the basic concept of instantaneous frequency (Huang and Wu 2008), IMF signals should meet two necessary conditions: (1) the same extreme value and zero crossing point in the entire data segment and (2) local symmetry relative to the time axis. The instantaneous frequency of the signal obtained in this way presents physical significance. Predefined IMF signals can be expressed as follows:

$$u_i(t) = p_i(t) \sin \phi_i(t), \quad (1)$$

where, $p_i(t)$ is the instantaneous amplitude, $p_i(t) \geq 0$, and $\phi_i(t)$ is the instantaneous phase, $\phi_i'(t) = \varphi_i(t) \geq 0$.

The spectrum of each IMF component is concentrated in a mode order-dependent center frequency φ_i . The following steps are performed to obtain the estimated bandwidth of the component (Dragomiretskiy and Zosso 2014).

(1) For each mode, compute the associated analytic signal by means of the Hilbert transform in order to obtain a unilateral frequency spectrum.

(2) For each mode, shift the mode's frequency spectrum to "baseband", by mixing with an exponential tuned to the respective estimated center frequency.

(3) The bandwidth is now estimated through the H^1 Gaussian smoothness of the demodulated signal, (i.e., the square L^2 norm of the gradient)

The above steps can be transformed into the following constrained variational problem:

$$\min_{\{u_i, \{\varphi_i\}\}} \left\{ \sum_i \left\| \hat{\sigma}t \left[\left(\delta(t) + \frac{j}{\pi t} \right) * u_i(t) \right] e^{-j\varphi_i t} \right\|_2^2 \right\} \quad (2)$$

The air shock wave signal is recorded as p , and the constraint of the variational problem is expressed as follows:

$$\sum_i u_i = p \quad (3)$$

A penalty factor α and Lagrange multipliers λ are introduced to render the variational problem unconstrained. In the Fourier frequency domain, the update expression of u_i and φ_i is directly optimized as:

$$\hat{u}_i^{n+1}(\varphi) = \frac{\hat{f}(\varphi) - \sum_{x < i} \hat{u}_i^{n+1}(\varphi) - \sum_{x > i} \hat{u}_i^n(\varphi) + \frac{\hat{\lambda}^n(\varphi)}{2}}{1 + 2\alpha(\varphi - \varphi_k^n)^2}$$

$$\varphi_i^{n+1} = \frac{\int_0^\infty \varphi |\hat{u}_i^{n+1}(\varphi)|^2 d\varphi}{\int_0^\infty |\hat{u}_i^{n+1}(\varphi)|^2 d\varphi} \quad (4)$$

The termination condition of the solution process is as follow:

$$\sum_i \|\hat{u}_i^{n+1} - \hat{u}_i^n\|_2^2 / \|\hat{u}_i^n\|_2^2 < \varepsilon \quad (5)$$

Through the above process, the original signal can be decomposed into several IMF's components expressed in sinusoidal form.

2.2 Energy Spectrum Calculation

The original air shock wave signal can be decomposed into several IMF components through the VMD algorithm. The instantaneous frequency spectrum of each shock wave component can be obtained through Hilbert transform. The Hilbert spectrum of the air shock wave signal can be obtained by synthesizing the instantaneous spectrum of all components (Ni *et al.* 2018). The Hilbert transform of IMF components can be expressed as follows:

$$H[u_i(t)] = \frac{1}{\pi} PV \int_{-\infty}^{+\infty} \frac{u_i(t')}{t-t'} dt', \quad (6)$$

where, PV represents the Cauchy principal value. The analytic expression of component signals can be constructed as follows:

$$z(t) = u_i(t) + jH[u_i(t)] = p(t)e^{j\varphi(t)}. \quad (7)$$

The following Hilbert spectrum can be considered the output of the air shock wave signal in a linear time-invariant system:

$$H(\varphi, t) = \text{Re} \sum_{i=1}^K p_i(t) e^{j \int \varphi_i(t) dt}. \quad (8)$$

Instantaneous energy spectrum (IE) and marginal energy spectrum (ES) can be obtained by integrating the square of $H(\varphi, t)$ with frequency and time, respectively. The instantaneous energy spectrum provides the change of air shock wave energy with time, and the marginal energy spectrum reflects each frequency component of the air shock wave that accounts for the global energy. IE and ES can be express as follows:

$$IE(t) = \int_0^{+\infty} H^2(\varphi, t) d\varphi, \quad (9)$$

$$ES(\varphi) = \int_0^T H^2(\varphi, t) dt. \quad (10)$$

3. TEST OF AIR SHOCK WAVE

3.1 Explosive and Test System

A 26 mm \times Φ 40 mm cylindrical TNT charge with a mass of 50 g was used in the test. The passivated RDX booster charge is set off with a #8 detonator. As shown in Fig. 1, the air shock wave overpressure test system is composed of TNT charge, pressure sensor, charge adapter, dynamic data acquisition instrument, low-noise cable, and portable computer. The test range of the pressure sensor is 0–10 MPa. The charge modulator is used to amplify the weak

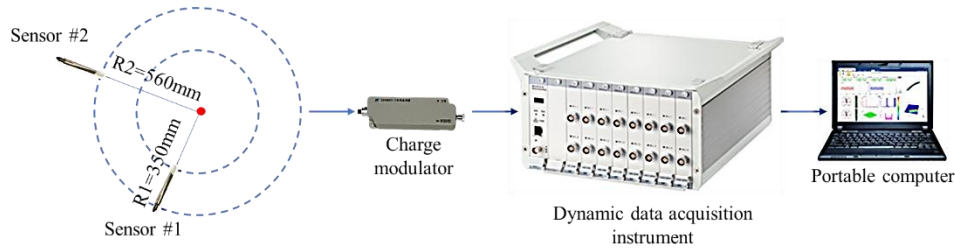


Fig. 1. Diagram of the air shock wave test system

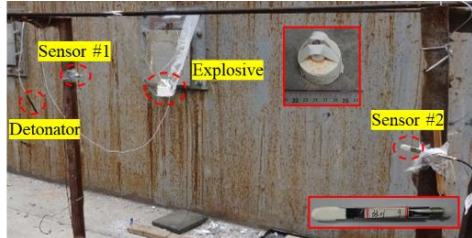


Fig. 2. Test layout for air shock wave.

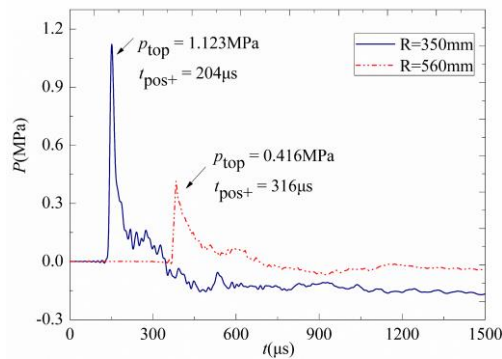


Fig. 3. Overpressure–time histories of the test.

charge signal tested by the sensor into a voltage signal, and the sampling frequency of the dynamic data acquisition instrument is 128 KHz.

3.2 Test Setup and Results

The TNT charge is hung in the air during the test. Pressure sensors #1 and #2 are fixed on the rigid support. The head of the pressure sensor is facing the explosion center, and the distance of pressure sensors #1 and #2 from the explosion center is 350 and 560

mm, respectively. Distances between the TNT charge, pressure sensor, and obstacles (such as ground, and wall) are greater than 1.5 m to eliminate the influence of obstacle reflection on the test results. The test layout is shown in Fig. 2. Overpressure–time histories at 350 and 560 mm are shown in Fig. 3. Pressure peak p_{top} and positive duration t_{pos+} are also marked in Fig. 3.

4. NUMERICAL SIMULATION OF AIR SHOCK WAVE

4.1 Finite element model

The limited number of waveforms obtained from the test can only reflect minimal information on the propagation laws of shock wave. Explicit fluid dynamic analysis code Ansys Autodyn can be used to supplement waveform data. Figure 4 shows the two-dimensional finite element model of the air shock wave from numerical simulation. One half finite element model is established for calculation given the symmetry of the actual situation. The TNT charge and air domain comprising the model adopt the Euler algorithm (Chen *et al.* 2007). The size of air domain is 2,000 mm × 1,000 mm, and the grid size is 2.5 mm × 2.5 mm. The size of the TNT charge in the model is 26 mm × 20 mm. A single point detonation is located at the center of the charge. Eight gauges are evenly arranged within the range of [150 mm, 500 mm] from the bottom of the charge to reflect the influence of the explosion distance on the overpressure histories. A gauge is placed at 350 and 560 mm from the charge center. The numerical and test results will be compared to validate the effectiveness of the proposed model.

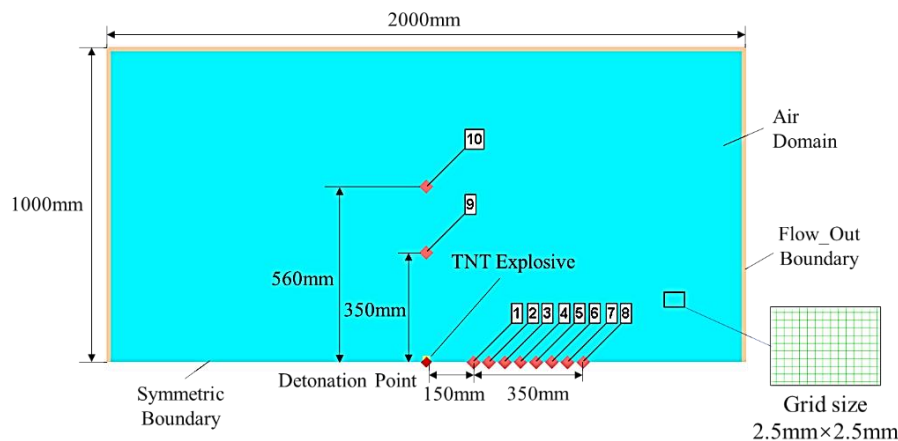


Fig. 4. Two-dimensional finite element model of air shock wave simulation.

4.2 Materials Model

The air adopts the following ideal gas model:

$$p = (k - 1)\rho e, \quad (11)$$

where, k is the adiabatic exponent with a value of 1.4. The initial density of air is 1.225 Kg/m^3 , and the initial internal energy is $2.068\text{E}5 \text{ J/Kg}$.

JWL equation of state is selected for the TNT explosive. The JWL model describes the detonation product expansion down to a pressure of 100 MPa for high energy explosive materials as follows:

$$p = A \left(1 - \frac{k\eta}{R_1} \right) e^{-\frac{R_1}{\eta}} + B \left(1 - \frac{k\eta}{R_2} \right) e^{-\frac{R_2}{\eta}} + k\rho e \quad (12)$$

where $\eta = \rho/\rho_0$, ρ_0 is the initial density of explosive, and ρ is the density of detonation product. The pressure of air shock wave decreases with the decrease of η during the expansion of detonation products. Values of constants A , B , R_1 , R_2 , and k are determined from dynamic experiments. The first two terms of Eq. (12) can be ignored after the pressure of the explosion product is less than 100 MPa. At this time, the JWL equation degenerates into the ideal gas equation. True density of TNT explosive used in the test is equal to $1,530 \text{ Kg/m}^3$. Initial parameters and JWL equation of state parameters of the explosive are listed in Table 1. Where, P_{CJ} is the C-J pressure of explosive, D is the detonation velocity, and e_0 is the initial specific internal energy.

Table 1 Initial parameters and JWL equation of state parameters of TNT

P_{CJ} (GPa)	D (m/s)	e_0 (KJ/m ³)	A (GPa)
18.5	6641	5.29×10^6	329.92
B (GPa)	R_1	R_2	k
3.3	4.15	0.9	0.35

4.3 Description of Validity of Simulation Results

Figure 5 presents the comparison between simulated and test waveforms at explosions distance of 350 and 560 mm, respectively. Waveforms showed that the simulation and test results are basically consistent. However, test waveforms demonstrate evident fluctuations due to the influence of environmental noise while simulated waveforms are closer to the ideal waveform. Simulated waveforms can accurately reflect the pressure discontinuity before and after the wave front. According to waveform characteristic parameters, the overpressure peak of simulated and test waveforms present relative errors of 1.24% and -6.12% , and those of 1.9% and 8.5% for the positive duration at an explosion distance of 350 and 560 mm, respectively. In conclusion, the

consistency between simulated and test waveforms proves the effectiveness of the numerical simulation results.

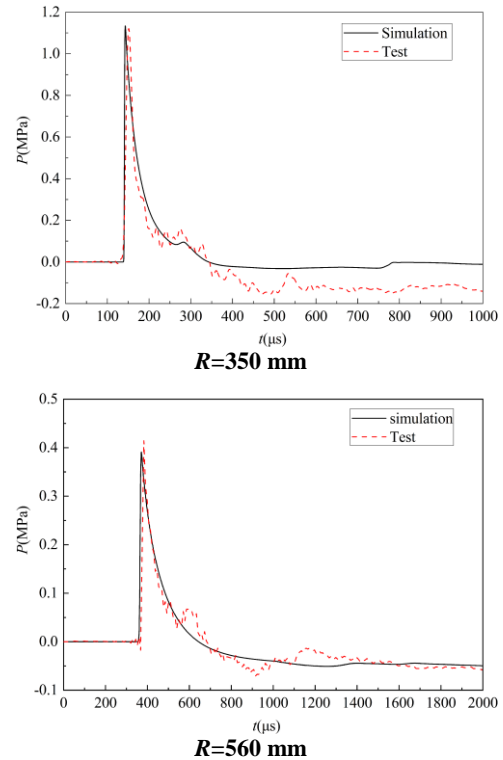


Fig. 5 Comparison of air shock waves obtained from simulation and test.

5. ENERGY EVOLUTION MECHANISM OF AIR SHOCK WAVE PROPAGATION AND ATTENUATION

5.1 Theoretical Analysis

Chemical explosions are characterized by rapid combustion accompanied by burned gas expansion. Mechanical energy of the detonation products expansion creates a blast wave that moves rapidly in the surrounding air. Blast wave represents an important property of an explosion. The blast wave affects the thermodynamic, state and dynamic of ambient air (pressure, density, particle velocity) (Isabelle 2018). According to the wave principle, particles in the air vibrate with the shock wave propagation while the density of air changes. Therefore, the energy of each point in the air also changes in the propagation process. The vibration of the shock wave causes the change of kinetic energy and the deformation causes the change of potential energy. The propagation process satisfies the following equations:

$$\begin{cases} \frac{\partial \rho}{\partial t} = -\nabla \cdot (\rho \vec{v}) \\ p = f(\rho, s) \\ \rho \left[\frac{\partial \vec{v}}{\partial t} + (\vec{v} \cdot \nabla) \vec{v} \right] = -\Delta p \end{cases} \quad (13)$$

Assuming that the propagation process of air shock wave is isentropic and the initial condition of air in Eq. (13) is zero. Ignoring the high-order small quantity, equations can be simplified as follows:

$$\begin{cases} \frac{\partial \rho}{\partial t} = -\nabla \cdot (\rho_0 \vec{v}) \\ \frac{\partial p}{\partial t} = c^2 \frac{\partial \rho}{\partial t} \\ \rho_0 \frac{\partial \vec{v}}{\partial t} = -\Delta p \end{cases} \quad (14)$$

The following wave equation of air shock wave can be derived from Eq. (14):

$$\frac{1}{c^2} \frac{\partial^2 p}{\partial t^2} - \nabla^2 p = 0. \quad (15)$$

Take any volume of air micro element V_0 , the micro element mass in still air is $m_0 = \rho_0 V_0$. The velocity of the micro element increases from 0 to v , and the volume of the micro element changes from V_0 to $V = m_0 / \rho$ when impacted by the shock wave. Kinetic energy E_k and potential energy E_p of the air can be expressed as follows:

$$E_k = \int_0^v m \frac{dx(t)}{dt} dv(t) = \frac{1}{2} \rho_0 V_0 v^2, \quad (16)$$

$$\begin{aligned} E_p &= -\int_{V_0}^V \Delta p dV \approx \int_{\rho_0}^{\rho} c^2 (\rho - \rho_0) d\rho \\ &= \frac{V_0}{2\rho_0} c^2 (\rho - \rho_0)^2 \end{aligned} \quad (17)$$

Due to $p = c^2 (\rho - \rho_0)$, the total energy density E is express as follows:

$$E = \frac{E_k + E_p}{V_0} = \frac{1}{2} \rho_0 v^2 + \frac{1}{2} \frac{p^2}{\rho_0 c^2}, \quad (18)$$

where p and v are functions of time.

The shock wave energy per unit volume on the wave front is defined as its energy flow density and denoted $\vec{\omega}$. According to the law of energy conservation of the micro-opening system, the net energy surplus in the system at any time is equal to the increase of the energy density of the system. That can be expressed as,

$$\frac{\partial E}{\partial t} = -\nabla \cdot \vec{\omega}. \quad (19)$$

Substitute Eq. (18) into Eq. (19) to obtain the following:

$$\frac{\partial E}{\partial t} = \rho_0 \vec{v} \cdot \frac{\partial \vec{v}}{\partial t} + \frac{1}{\rho_0 c^2} p \frac{\partial p}{\partial t}. \quad (20)$$

Substitute Eq. (14) into Eq. (20):

$$\frac{\partial E}{\partial t} = -\vec{v} \cdot \nabla p - p \nabla \cdot \vec{v} = -\nabla \cdot (p \vec{v}),$$

$$\text{That is, } \vec{\omega} = p \vec{v}. \quad (21)$$

The average value of the energy flow density in a period T is called the average energy flow density. Thus, the average energy flow density I of the air shock wave is expressed as

$$I = \frac{1}{T} \int_0^T p v dt. \quad (22)$$

Given the three-dimensional wave equation is complicated, the energy change of the one-dimensional shock wave is discussed here. The wave equation is

$$\frac{1}{c^2} \frac{\partial^2 p}{\partial t^2} - \frac{\partial^2 p}{\partial x^2} = 0. \quad (23)$$

The classic solution of the one-dimensional wave equation is

$$p(x, t) = f(x - ct) = \rho_0 c v(x - ct), \quad (24)$$

$$\begin{aligned} v(x, t) &= -\frac{1}{\rho_0} \int \frac{\partial f}{\partial x} dt = \frac{1}{\rho_0 c} f(x - ct) \\ &= \frac{1}{\rho_0 c} p(x, t) \end{aligned} \quad (25)$$

The waveform of air shock wave is the solution of wave equation at a certain position. We substitute the analytical expression (Eq. (5)) of the harmonic decomposition of the air shock wave obtained by VMD into Eqs. (24) and (25) to obtain the following:

$$p_i(x, t)|_{x=R} = p_i(t) e^{j\phi_i(t)},$$

$$v_i(x, t)|_{x=R} = \frac{1}{\rho_0 c} p_i(t) e^{j\phi_i(t)},$$

$$\begin{aligned} I_i &= \frac{1}{T} \int_0^T \text{Re}[p_i(x, t)] \cdot \text{Re}[v_i(x, t)] dt \\ &= \frac{1}{2} \rho_0 c \varphi_i^2 \varepsilon_{ief}^2 \end{aligned} \quad (26)$$

where, ε_{ief} is the equivalent displacement under IMF component load, and is proportional to the pressure peak of the component. Thus, the energy of IMF component is proportional to the second power of the amplitude and frequency of the component. The energy of high-frequency waves is greater than that of low-frequency waves in the propagation period under the same amplitude. The harmonic components of different frequencies satisfy the principle of superposition given that the wave equations of harmonic components present linear properties. Therefore, the energy of air shock wave is also proportional to the second power of its amplitude.

The above analysis on the propagation process of air shock wave is based on the plane wave assumption. However, the actual air shock wave propagates outwards in the form of a spherical wave. Energy absorption is accompanied by spherical propagation, which will cause the geometric and absorption attenuations of the shock wave energy. As shown in

Fig. 6, the non-spherical charge also propagates outward in the form of a near-spherical wave after the propagation distance exceeds a certain range. Figure 6 presents that the shock wave becomes spherical at 40 μs , and the distance from the explosion center is 130 mm. Hence, the range from the bottom of the charge of [150 mm, 500 mm] belongs to the category of spherical waves. Landau pointed out that the average energy flow density of the spherical shock wave is inversely proportional to the volume contained in the wave (Vladimir 2018). Thus, the decrease of average energy flow density of air shock wave is inversely proportional to the third power of the distance traveled by the wave. The relationship of frequency in the process of geometric attenuation is expressed as follows (He and Zhao 1981):

$$\varphi_p = \gamma_p \cdot \frac{c}{2\pi R}, \quad (27)$$

where γ_p is a constant. Equation (25) shows that frequency is related to the velocity of the spherical wave and the propagation distance. The decrease of the wave velocity and the increase of the propagation distance will reduce the frequency. The absorption attenuation of the shock wave can be expressed as follows (Allan 1980):

$$p(x) = p \cdot e^{-\beta x}. \quad (28)$$

where β is the attenuation coefficient. Absorption attenuation coefficients of viscous and the heat conduction absorptions are expressed as follows (Allan 1980):

$$\text{Viscous absorption } \beta \approx \frac{\varphi^2 \nu}{2c_0^3}, \quad (29)$$

Heat conduction absorption

$$\beta = \frac{\varphi^2}{2\rho_0 c_s^3} \frac{\chi(\gamma-1)}{c_v \gamma}, \quad (30)$$

where $\gamma = c_p / c_v$, χ is the heat conduction absorption coefficient, and c_s is the wave velocity in the adiabatic process. Therefore, the absorption attenuation coefficient of the air shock wave either viscous or heat conduction absorption is directly proportional to the square of its frequency. The absorption attenuation of high-frequency shock waves is remarkably greater than that of low-frequency shock waves.

5.2 Waveforms and Frequency Spectra of Air Shock Wave at Different Explosion Distances

Shock wave waveforms at different explosion distances are shown in Fig. 7, where H represents the distance from the gauge to the bottom of the charge. The calculation results in Fig. 7 effectively reflect the process of change of air shock wave waveforms. The overall trend in the propagation process of the air shock wave is attenuating. The pressure peak gradually decreases with the increase of the explosion distance while the positive duration gradually increases because the wave front is a shock wave while the wave rear is a continuous wave. The shock wave compresses air, so the propagation velocity of the wave front is greater than that of the undisturbed medium. However, the continuous wave restores the air to its original state, hence the propagation velocity of the wave rear is less than the sound velocity of gas in the initial state. As a result, the velocity of the wave front is greater than that of the wave rear. Therefore, the distance between the wave front and the wave rear increases with time, resulting in the increase of the width of the shock wave.

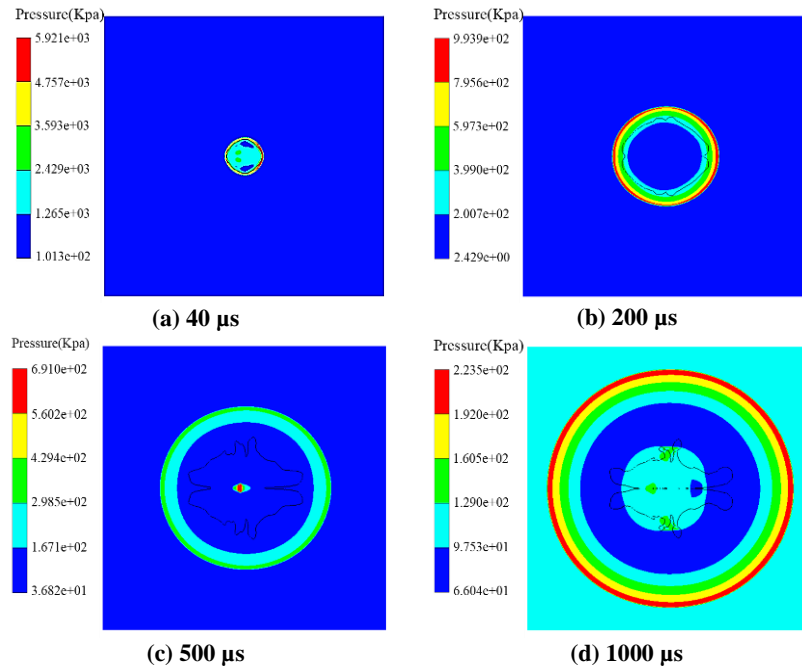


Fig. 6. Cloud diagram of pressure change of air shock wave at different moments.

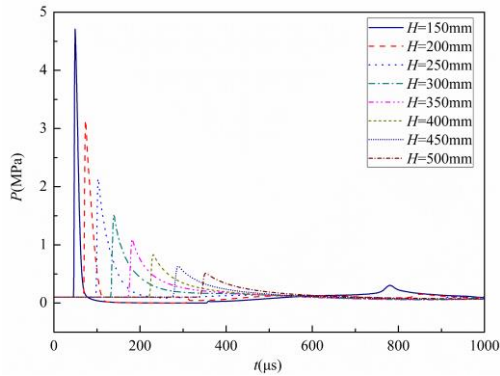


Fig. 7. Waveforms of Air shock wave at different explosion distances.

The amplitude spectrum of air shock waves shown in Fig. 7 is computed using fast Fourier transform (FFT). The calculation results are presented in Fig. 8. The continuous frequency spectrum of the air shock wave reflects the contribution or proportion of different frequency components to the signal. The component near zero frequency presents the maximum proportion in the shape of the amplitude spectrum because the constant atmospheric pressure is superimposed on the simulated waveforms. Although the amplitude spectrum is generally high in the frequency range of 0–1,000 Hz, it shows a rapid decreasing trend. Amplitude – frequency curves of the air shock wave at different explosion distances begin to separate in the frequency range of 1,000–60,000 Hz, and the amplitude value of the small distance is evidently greater than that of the large distance. The decreasing trend of the amplitude spectrum slows down and the amplitude frequency curves of air shock wave with different explosion distances gradually approach at values as the frequency is greater than 60,000 Hz. This analysis shows that the difference in the amplitude of the air shock wave at different explosion distances is mainly reflected in the range of 1,000–60,000 Hz as the propagation distance increases.

5.3 Energy distribution of air shock wave based on energy spectra

Initial parameters such as penalty factor, modal decomposition number, fidelity coefficient, and convergence condition should be set in advance when the VMD algorithm is used to decompose air shock wave signals. The modal decomposition number i and the penalty factor α exert the maximum significant influence on the decomposition accuracy. VMD is an adaptive decomposition algorithm with solid theoretical foundation. The convergence of VMD is determined by the initial parameters. When the initial parameters are selected, the decomposition result is convergent, which has been proved in Dragomiretskiy and Zosso (2014). Therefore, the convergence verification is not necessary. The method of choosing initial parameters of VMD can be obtained from Li *et al.*(2016) and Sun *et al.* (2020). In this paper, the fidelity coefficient and convergence condition are set as default values, and $i=5$ and, α

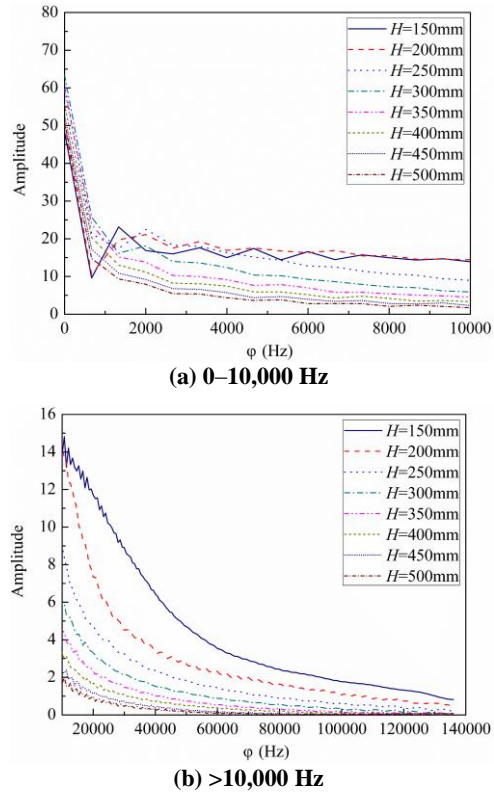


Fig. 8. Amplitude distribution of air shock wave in the frequency domain

$=0.4 L$ are selected for calculation, where L is the signal length. The decomposed sub signal satisfies the convergence condition and correlation condition (Li *et al.* 2016). The Hilbert spectrum of air shock waves can be obtained by substituting the shock wave waveforms shown in Fig. 7 into Eqs. (1)– (8). Equation (9) shows that the instantaneous energy spectrum of air shock waves can be calculated by integrating the square of Hilbert spectrum with the frequency. Figure 9 illustrates the instantaneous energy spectrum at 250 mm from the bottom of the charge and reflects the change of air shock wave energy with time. The time of the instantaneous energy peak is consistent with that of the pressure peak. Statistics of pressure peaks p_{top} and the instantaneous energy peaks IE_{top} of the air shock waves are listed in Table 2.

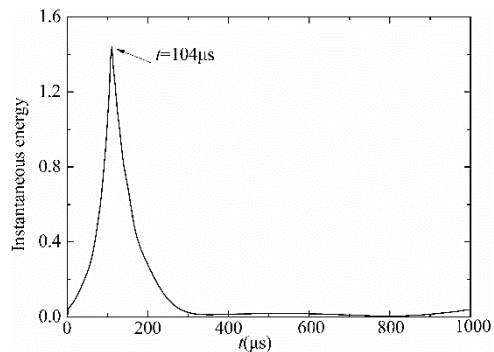


Fig. 9. Instantaneous energy spectrum of air shock wave when $H=250$ mm.

Table 2 Instantaneous energy and pressure peaks of air shock waves at different distances

$H(\text{mm})$	p_{top} (MPa)	IE_{top}
150	4.71	4.85
200	3.14	2.66
250	2.14	1.41
300	1.51	0.76
350	1.10	0.43
400	0.83	0.26
450	0.63	0.15
500	0.51	0.10

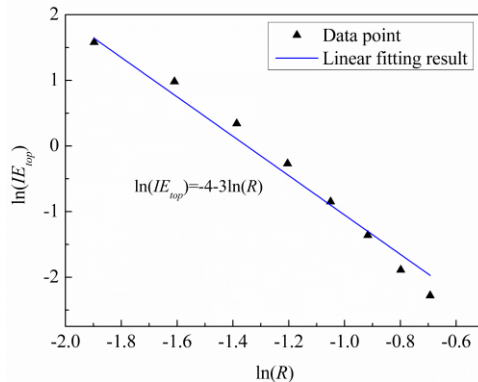


Fig. 10. Relationship between instantaneous energy peak of air shock wave and explosion distance.

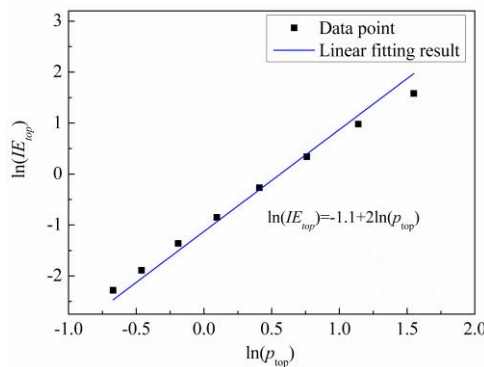


Fig. 11. Relationship between instantaneous energy and pressure peaks of air shock wave.

Analyzing the statistical data in Table 2, Fig. 10 demonstrates that the instantaneous energy peak of air shock wave is inversely proportional to the third power of explosion distance. This finding is consistent with that of Landau (Vladimir, 2018). The results in Fig. 11 showed that the instantaneous energy peak of the air shock wave is nearly proportional to the square of the pressure peak. The consistency between this conclusion and the result of Eq. (26) proves the correctness of the VMD harmonic decomposition model. Equation (10) shows that the marginal energy spectrum of air shock waves can be obtained by integrating the square of Hilbert spectrum with time. Figure 12 presents the marginal energy spectrum at 250 mm from the bottom of the charge that reflects the change of air

shock wave energy with frequency. Compared with the amplitude spectrum shown in Fig. 8, the marginal energy spectrum can better reflect the concentration trend of air shock wave energy, highlight local time–frequency characteristics of the signal, and avoid false components caused by continuous Fourier transform. It can be also found by comparing Fig. 8 and Fig. 12 that the amplitude of signal component near 10000 Hz is smaller than that of 0–1000 Hz, but the energy is higher. This phenomenon is caused by the joint determination of the signal energy using the amplitude and frequency, and consistent with the result of Eq. (24).

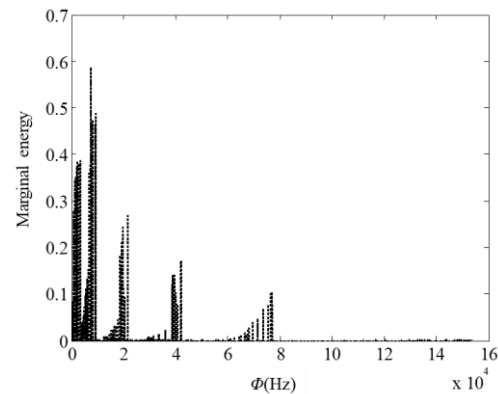


Fig. 12. Marginal energy spectrum of air shock wave when $H=250$ mm.

According to the change trend of the amplitude spectrum (Fig. 8), the marginal energy spectrum of each air shock wave is divided into several segments. The statistical results illustrated in Fig. 13 can be obtained by adding the marginal energy of each frequency in each segment. The statistical results intuitively reflect the attenuation law of air shock wave energy under different explosion distances. The attenuation rate of air shock wave energy gradually decelerates. The energy of different frequency bands is different, and the frequency band with the maximum energy at different explosion distances also varies. The maximum frequency band of air shock wave energy gradually shifts from high frequency to low frequency as the explosion distance increases. This phenomenon is caused by a nonlinear attenuation called dispersion of air shock wave. The frequency dispersion phenomenon reduces the frequency of the air shock wave. The attenuation rate of the total shock wave energy becomes increasingly slow because the attenuation coefficient of the wave decreases as the frequency decreases.

6. CONCLUSION

The energy evolution mechanisms of air shock wave in the propagation and attenuation process were investigated on the basis of fluid wave theory and energy spectrum analysis. Distribution laws of shock wave energy with time, frequency and explosion distance were also determined. The following conclusions can be drawn from this study:

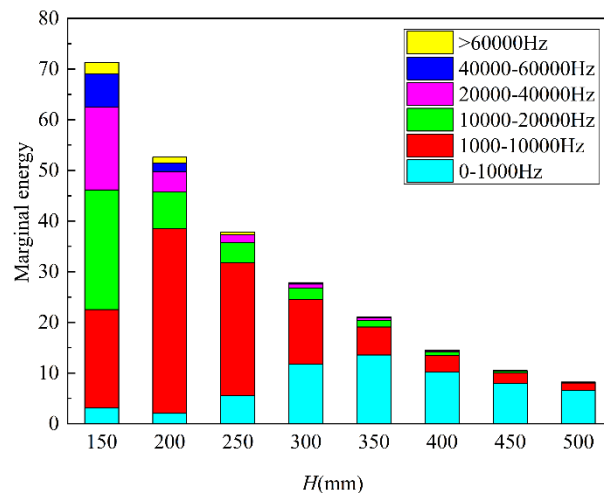


Fig. 13. Energy spectrum distribution of air shock wave at different explosion distances.

(1) Instantaneous and marginal energy spectra of the air shock wave reflect the time–frequency evolution laws of its energy. The consistency between the calculated results combined with VMD and Hilbert transform and theoretical results verified that VMD and Hilbert transform are powerful tools in the investigation of the time–frequency distribution of air shock wave energy.

(2) The energy of harmonic components of air shock wave is jointly determined by the amplitude and frequency, and directly proportional to the square of the amplitude and frequency. Moreover, the instantaneous energy peak of air shock wave at any position is directly proportional to the square of its pressure peak because the wave equation of harmonic components satisfies the superposition principle.

(3) Geometric and absorption attenuation mechanisms are observed when the shock wave propagates in the air. The instantaneous energy peak of the shock wave is inversely proportional to the third power of the propagation distance and the energy attenuation rate of the high-frequency component is faster due to the two attenuation mechanisms.

(4) The frequency dispersion caused by the nonlinear attenuation of air shock wave results in the transfer of the maximum energy band of the marginal energy spectrum from high frequency to low frequency. Therefore, the attenuation rate of total energy will gradually decelerate in the propagation process of the shock wave.

The instantaneous and marginal energy spectra intuitively reflect the time-frequency characteristics of air shock wave energy, providing powerful tools for explaining the propagation phenomena of shock wave (such as attenuation, and dispersion). In the follow-up researches, it can also be used to explain the reflection and transmission of shock wave at the structural interface and the propagation laws of shock wave in complex environment.

ACKNOWLEDGEMENTS

The authors would like to acknowledge National Natural Science Foundation of China (Grant No. 11872214) and Postgraduate Research & Practice Innovation Program of Jiangsu Province (Project No. KYCX20_0313) to provide fund for conducting experiments.

REFERENCES

- Allan D. P. (1980). *Acoustics: An Introduction to Its Physical Principles and Applications*. the Acoustical Society of America.
- Anderson, J. G., G. Katselis and C. Caputo (2000). *Analysis of a generic warhead part 1: experimental and computational assessment of free field overpressure*. DSTOTR-1313. Australia: Defence Science and Technology Organization.
- Artero-Guerrero, J., J. Pernas-Sánchez and F. Teixeira-Dias (2017). Blast wave dynamics: The influence of the shape of the explosive. *Journal of Hazardous Materials* 331, 189-199.
- Bowles, T., D. Stevens and M. Stanley (2012). *Blast Loads in and Urban Environment*: Structures Congress 2012. 201270-79.
- Brode, H. L. (1955). Numerical solutions of spherical blast waves. *Journal of Applied Physics* 26(6), 766-75.
- Chen, J., H. K. Ching and F. Allahdadi (2007). Shock-induced detonation of high explosives by high velocity impact. *Journal of Mechanics of Materials and Structures* 2(9), 1701-1721.
- Cooper, G. J. and D. E. M. Taylor (1989). Biophysics of Impact Injury to the Chest and Abdomen. *BMJ Military Health*. 135, 58-67.
- Dragomiretskiy, K. and D. Zosso (2014). Variational Mode Decomposition. *IEEE Transactions on*

- Signal Processing* 62(3), 531-544.
- Fouchier, C., D. Laboureur, L. Youinou, E. Lapebie and J. Buchlin (2017). Experimental investigation of blast wave propagation in an urban environment. *Journal of Loss Prevention in the Process Industries* 49, 248-265.
- Friedlander, F. G. (1946). The diffraction of sound pulses. I. Diffraction by a semi-infinite plate. *Proceedings of the Royal Society of London A* 186, 322-344.
- Goel, M. D. (2015). Blast: Characteristics, Loading and Computation—An Overview. In: Matsagar V. (eds) *Advances in Structural Engineering*. Springer, New Delhi.
- He, Z. Y. and Zhao Y. F. (1981). *Fundamental of acoustic theory*. National Defense Industry Press.
- Held, M. (1983a). Blast waves in free air. *Propellants, Explosives, Pyrotechnics* 18(1), 1-8.
- Held, M. (1983b). TNT-Equivalent. *Propellants, Explosives, Pyrotechnics*. 8, 158-167.
- Henrych, J. (1979). *The dynamics of explosion and its use*. Elsevier, Amsterdam.
- Hong, X., W. Li and W. Li (2020). Energy Spectrum of Explosion Shock Wave Signals of Multi-layer Composite Charge. *ACTA ARMAMENTARII* 41(11), 2243-2251.
- Huang, N. E. and Wu Z. (2008). A review on Hilbert-Huang transform: Method and its applications to geophysical studies. *Reviews of Geophysics*. 46(2), G2006.
- Isabelle, S. (2018). *Blast Effects: Physical Properties of Shock Waves*. Springer Nature.
- Izadifard, R. A. and M. Foroutan (2010). Blast wave parameters assessment at different altitude using numerical simulation. *Turkish journal of engineering & environmental sciences* 34(1), 25-41.
- Kinney, G. F. and K. J. Graham (1985). *Explosive shocks in air*. Springer, Berlin.
- Kong, L., J. Su and Z. Li (2010). Energy Spectrum Analysis of Several Kinds of Explosive Blast. *Chinese Journal of Explosives & Propellants*.
- Li, L., F. Wang, F. Shang, Y. Jia, C. Zhao and D. Kong (2017). Energy spectrum analysis of blast waves based on an improved Hilbert–Huang transform. *Shock Waves* 27(3), 487-494.
- Li, M., J. Jiang and X. Wang (2018). Shock wave propagation characteristics of double layer charge explosion in the air. *Explosion and Shock Waves* 38 (2), 367-372.
- Li, X., Y. Ma and S. Li (2019). Research on Frequency Distribution of Peak Area of Blast Shock Wave. *Transactions of Beijing Institute of Technology* 39(02), 125-130.
- Li, Z., J. Chen, Y. Zi, J. Pan and Y. Wang (2016). Improved VMD for feature visualization to identify wheel set bearing fault of high-speed locomotive. *IEEE Instrumentation and Measurement Technology Conference*.
- Maiz, L., W. Trzciński, M. Szala, J. Paszula and K. Karczewski (2016). Studies of Confined Explosions of Composite Explosives and Layered Charges. *Central European Journal of Energetic Materials* 13(4), 957-977.
- Ni, P., J. Li, H. Hao, Y. Xia, X. Wang and J.M. Lee (2018). Time-varying system identification using variational mode decomposition. *Structural Control and Health Monitoring* 25(6).
- Silnikov, M. V., M. V. Chernyshov and A. I. Mikhaylin (2015). Blast wave parameters at diminished ambient pressure. *Acta Astronautica* 109, 235-240.
- Simoens, B. and M. Lefebvre (2015, December). Influence of the Shape of an Explosive Charge: Quantification of the Modification of the Pressure Field. *Central European Journal of Energetic Materials*.
- Sun, M. and L. Zhi (2020). Modal parametric identification of building structures based on VMD. *Journal of Vibration and Shock* 39(01), 175-183, 190.
- Thornhill, C. K. (1959). *The shape of a spherical blast wave*. Armament Research and Development Establishment (ARDE) Memo. (B) 41/59. London: HMSO.
- UFC-3-340-02 (2008). Structures To Resist The Effects Of Accidental Explosions. US Department of Defense (DOD).
- Vladimir, F. (2018). *Intense Shock Waves on Earth and in Space*. Moscow Fizmatlit.
- Wang, C., Z. Liu, L. Gao, D. Xu and Z. Zhuang (2017). Analytical and numerical modeling on resonant response of particles in polymer matrix under blast wave. *Computational Materials Science* 140, 70-81.
- Zhang, E., G. Lu and H. Yang (2020). Band gap features of metaconcrete and shock wave attenuation in it. *Explosion and Shock Waves* 40(06), 69-77.